Nano Energy 154 (2026) 111991

Contents lists available at ScienceDirect

Nano Energy

journal homepage: www.elsevier.com/locate/nanoen

Full paper

Triboelectric-induced polarization directing molecular self-assembly without chemical functionalization

Yu Wei [a,b,1], Xiang Li [a,b,1], Bobo Sun [a,b], Lixue Yang [a], Jiajia Shao [a], Zhong Lin Wang [a], Di Wei [a,c,*]

[a] Beijing Institute of Nanoenergy and Nanosystems, Chinese Academy of Sciences, Beijing, PR China
[b] School of Nanoscience and Engineering, University of Chinese Academy of Sciences, Beijing, PR China
[c] Centre for Photonic Devices and Sensors, University of Cambridge, 9 JJ Thomson Avenue, Cambridge, UK

ARTICLE INFO

Keywords:
Triboelectric-induced polarization
Self-assembly
Layer-by-layer
Contact electrification

ABSTRACT

Molecular self-assembly is a central bottom-up route for constructing functional interfaces, yet most strategies rely on predefined surface chemistries, stringent environmental control, or externally applied fields, which limit robustness and scalability. Here we demonstrate that triboelectric-induced polarization can act as a mechanically generated, bias-free interfacial electric field to direct molecular organization in solution. Triboelectric-induced polarization on a fluorinated ethylene propylene (FEP) platform produces a stable and directional polarization field that drives the sequential adsorption and layer-by-layer (LbL) assembly of oppositely charged polyelectrolytes, enabling the formation of a well-defined polyethyleneimine (PEI)/alginate (ALG) multilayer without surface functionalization or external voltage. Systematic electrical, wetting, spectroscopic, and microscopic characterizations collectively confirm the field-enabled assembly mechanism and elucidate the resulting interfacial architecture and chemical composition. Beyond mechanistic validation, the as-formed PEI/ALG interface demonstrates rapid underwater oil detachment, highlighting its functional relevance for self-cleaning surfaces. Together, these results identify triboelectric-induced polarization as a programmable physical parameter for directing interfacial molecular assembly, providing an energy-autonomous route to adaptive and functional coatings operable under minimal environmental constraints.

1. Introduction

Molecular self-assembly underpins a broad range of functional materials and interfaces [1–3], enabling bottom-up construction across molecular [4,5], nanoscale [6,7], and mesoscale regimes [8,9]. By harnessing noncovalent interactions [10], including electrostatic forces [11–13], hydrogen bonding [14–16], van der Waals interactions [17,18], and coordination chemistry [19,20], self-assembly has facilitated advances in membranes [21], coatings [22], photonic structures [23], and adaptive surfaces [24]. Despite notable advances, most self-assembly strategies remain fundamentally constrained by their dependence on predefined chemical functionalities [25,26], externally applied fields [27,28], or highly controlled and geometry-limited environments [29,30]. Chemically driven approaches often suffer from limited adaptability and scalability, reduced environmental tolerance, and increased fabrication complexity, while also posing risks of contamination and irreversible surface modification. Electric fields provide a powerful alternative by reshaping interfacial free-energy landscapes and directing the organization of charged or polar building blocks. Accordingly, electric control has been widely employed in layer-by-layer (LbL) assembly [31], electrochemical deposition [32], and field-assisted adsorption processes [33]. However, these methods typically rely on continuous external power sources, rigid electrode configurations, or conductive substrates, which restrict practical deployment and, critically, decouple mechanical interactions from molecular organization. A key unresolved challenge therefore lies in generating spatially structured and directional interfacial electric fields in a power-free, materials-agnostic manner, while maintaining sufficient field strength to actively regulate molecular assembly.

Contact electrification (CE) provides a compelling yet underexplored solution to this challenge [34–37]. When two materials come into contact and separate, charge transfer occurs at the interface, giving rise to

---

* Corresponding author at: Beijing Institute of Nanoenergy and Nanosystems, Chinese Academy of Sciences, Beijing, PR China.
E-mail address: weidi@binn.cas.cn (D. Wei).

[1] These authors contributed equally to this work

https://doi.org/10.1016/j.nanoen.2026.111991
Received 12 March 2026; Received in revised form 14 April 2026; Accepted 24 April 2026

long-lived surface charges and an accompanying electrostatic field [38,39]. Traditionally regarded as an incidental or parasitic phenomenon, CE has recently been re-envisioned as a robust physical mechanism for mechanically generating interfacial electric fields with strengths comparable to those produced by externally applied electrical biases [40,41]. This concept underpins the operation of triboelectric nanogenerators (TENGs), where interfacial charge transfer is harnessed to convert mechanical energy into electrical output, further highlighting the capability of CE to establish and sustain functional electrostatic fields at interfaces [42,43]. Beyond energy harvesting, recent studies have extended this principle to CE-enabled interfacial processes, such as CE-induced catalysis, where mechanically generated charges actively modulate interfacial reactions and charge-transfer dynamics [44,45]. These advances highlight the broader potential of triboelectricity as a versatile means of interfacial charge and polarization regulation. Crucially, the resulting triboelectric-induced polarization field is inherently non-contact, electrode-free, and self-sustained, emerging directly from mechanical interactions at the interface rather than from external power sources. This intrinsic coupling between mechanical motion and electrostatic field generation distinguishes CE from conventional electrostatic approaches and enables programmable interfacial fields under minimal material and environmental constraints. Beyond static charge accumulation, such fields have been shown to modulate electrical double layers (EDLs) [46–48], gate ionic transport, and couple mechanical stimuli to charge redistribution and the flow of energy and information [49,50], providing a unique means of regulating interfacial processes in a fully passive manner [51,52]. Triboelectric-induced polarization provides a versatile platform for dynamically regulating ion distributions within nanoconfined EDLs [53,54]. By directly coupling mechanical and fluidic stimuli to interfacial charge redistribution, this mechanism enables efficient energy conversion through enhanced ionic-electronic interactions [55–57], while simultaneously supporting a broad spectrum of information-processing functions, including signal detection and storage [56,58,59], logic operations [60], synapse-like behavior [61], and underwater wireless communication [62]. Despite these advances, the potential of triboelectric-induced polarization to actively regulate molecular self-assembly has remained largely unexplored. Existing electrostatic assembly strategies predominantly rely on externally imposed electric fields or predefined surface chemistries to dictate molecular pairing and ordering. In contrast, mechanically generated polarization fields exhibit fundamentally distinct attributes, including intrinsic spatial nonuniformity, directionality determined by interfacial charge asymmetry, and dynamic tunability governed by mechanical stimuli. These characteristics suggest that triboelectric-induced polarization can reshape local ionic distributions remotely, modulate charge-compensation environments, and establish long-range electrostatic gradients capable of directing molecular organization without chemical functionalization or external bias. Harnessing such fields for self-assembly thus represents not merely an alternative driving force, but a paradigm shift in which mechanical interactions are directly transduced into chemical order.

Here, a molecular self-assembly strategy driven by triboelectric-induced polarization was demonstrated, in which mechanically generated interfacial electric fields guide molecular adsorption and LbL assembly of oppositely charged polyelectrolytes in a power-free manner. Using polyethyleneimine (PEI) and alginate (ALG) as representative polycationic and polyanionic building blocks, respectively, it is demonstrated that triboelectric-induced polarization can drive their sequential organization into stable multilayer architectures on FEP/Au substrates, without the need for surface functionalization or externally applied voltages. Through integrated surface potential measurements, spectroscopic analyses, and microscopic characterizations, a direct mechanistic correlation between triboelectric-induced polarization and interfacial molecular organization is established. Collectively, these results identify triboelectric-induced polarization as a programmable physical variable for molecular assembly, providing a generalizable strategy for constructing adaptive interfaces, autonomous materials, and mechanically coupled energy-matter-information systems remotely.

2. Results and discussion

2.1. Molecular self-assembly driven by electric fields from triboelectric-induced polarization

CE originates from interfacial charge transfer that occurs when two materials come into intimate contact and subsequently separate. At the microscopic level, this process can be rationalized by the electron cloud-potential well model, in which atoms or molecules are regarded as potential wells confining delocalized valence electrons. As two solids approach each other, the interfacial separation decreases, and their electron clouds begin to overlap, distorting the initially symmetric potential wells into an asymmetric double-well configuration (Fig. S1). Differences in electronic structure, such as work function mismatch, render one side energetically favorable for electron occupation, enabling electrons to tunnel across the interfacial barrier. This interfacial electron transfer establishes opposite charges on the contacting surfaces, giving rise to persistent surface polarization after separation.

Building on this mechanism, we designed a triboelectric-induced polarization interface capable of generating a stable, directional electric field to drive molecular self-assembly. As illustrated in Fig. 1A, a thin Au layer was deposited on one side of a fluorinated ethylene propylene (FEP) film, while the opposite side was subjected to triboelectric interaction with fur material. Upon repeated contact and sliding, triboelectric charge transfer led to the accumulation of negative charges on the FEP surface and corresponding positive charges on the fur. The conductive Au layer functions as an electrostatic boundary that facilitates charge redistribution and enables reliable characterization of the polarization field [63], while the molecular assembly is governed by the dielectric substrate and does not rely on specific chemical interactions with Au. The spatial separation of triboelectric charges establishes a polarization field across the FEP/Au structure, oriented toward the negatively charged FEP surface (Fig. 1A I-III). This interfacial field serves as the driving force for subsequent ion redistribution and molecular adsorption near the interface, thereby enabling field-directed self-assembly. Importantly, this electric field is generated mechanically, without external bias or electrodes, and persists long enough to interact with species in the surrounding environment. When the triboelectric-induced polarization FEP/Au was immersed in an aqueous solution containing positively charged molecules, the polarization field acted as a long-range driving force that guided cationic species toward the interface. Under the influence of this field, positively charged molecules migrated directionally and adsorbed onto the FEP/Au surface, forming a stable positively charged molecular layer (Fig. 1A IV). Subsequent immersion of this modified surface into a solution containing negatively charged molecules resulted in electrostatically driven adsorption of anionic species onto the preassembled cationic layer, yielding a negatively charged overlayer (Fig. 1A V). Through this mechanism, triboelectric-induced polarization converts mechanical stimulation into an effective interfacial electric field that directs sequential molecular organization, enabling self-assembly without surface functionalization or externally applied electric fields.

Experimentally, this process was implemented through a simple sequential dipping protocol (Fig. 1B). The FEP/Au film was first triboelectric-induced polarization by triboelectric with fur, then immersed in a solution containing the first molecular building block for 2 min to allow field-driven adsorption. After rinsing with deionized water to remove weakly bound species, the sample was immersed in a second molecular solution for an additional 2 min, followed by rinsing and drying. Repetition of this process enabled LbL interfacial molecular assembly driven entirely by triboelectric-induced polarization, without additives, chemical modification, or external power input. To demonstrate this concept, PEI and ALG were selected as representative

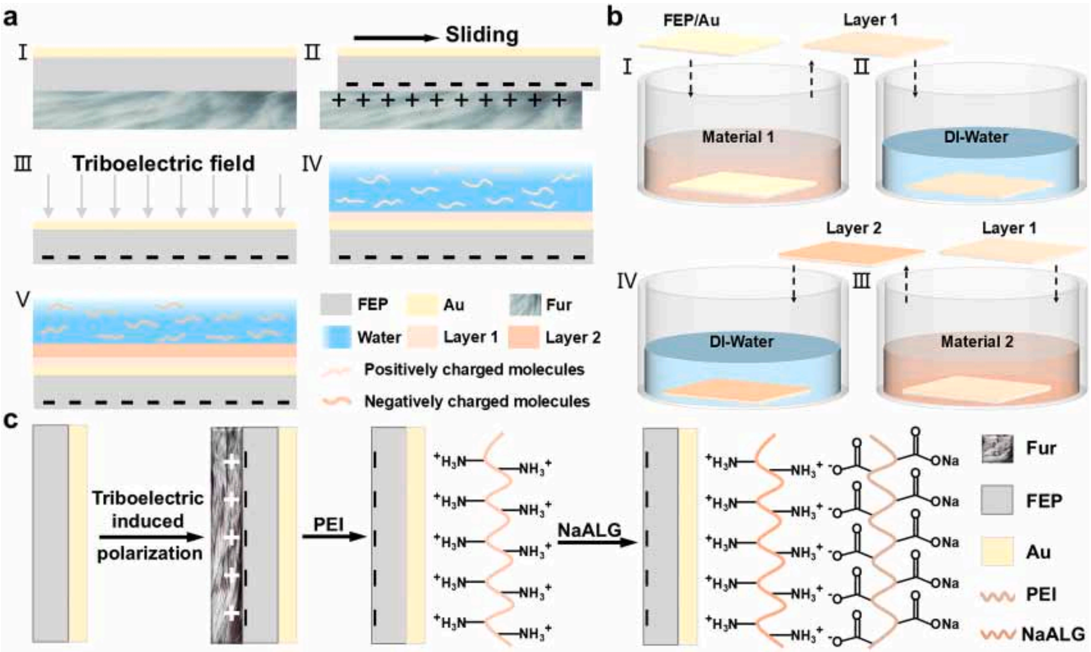

Fig. 1. Triboelectric-induced polarization molecular self-assembly. (A) Triboelectric-induced polarization generates an interfacial electric field at the FEP/Au interface, enabling adsorption of charged molecules through electrostatic interactions. (B) Alternating exposure of the polarized interface to oppositely charged molecular solutions realizes a stepwise LbL self-assembly process without external electrical bias. (C) PEI and ALG with complementary charge characteristics enable sequential assembly driven by triboelectric-induced polarization.

polycationic and polyanionic building blocks, respectively (Fig. 1C). PEI contains a high density of amine groups that readily protonate in aqueous environments, generating positively charged -NH_3^+ species and imparting strong cationic character (Fig. S2). In contrast, ALG is a linear polysaccharide bearing carboxyl groups that deprotonate to form negatively charged -COO^- groups under neutral conditions, resulting in pronounced anionic behavior. The complementary charge characteristics of PEI and ALG make them an ideal model system for probing triboelectric-induced polarization-directed molecular assembly. Importantly, in this system, the sequential organization of PEI and ALG is not dictated by predefined surface chemistry, but rather by the mechanically generated interfacial electric field, highlighting triboelectric-induced polarization as an active physical variable for directing molecular self-assembly.

2.2. *Triboelectric-induced polarization-directed self-assembly of PEI*

To quantify whether triboelectric-induced polarization generates an interfacial electric field that is sufficiently strong and stable to drive adsorption, we first measured the surface potential of the Au layer in the FEP/Au structure after triboelectric with fur. As shown in Fig. 2A, the Au surface potential became increasingly negative with increasing triboelectric duration, indicating progressive accumulation of triboelectric charges and strengthening of the polarization field. The potential approached a steady value after ~60 s of triboelectric, suggesting that the triboelectric charging process reached a quasi-saturation regime under the applied mechanical conditions. To evaluate the repeatability and durability of the triboelectric-induced polarization field, multiple independent triboelectrification cycles were performed under identical conditions, yielding highly consistent surface potentials (Fig. S3), which demonstrates reliable generation of the polarization field. Time-dependent measurements further show that, although the surface potential gradually decreases due to charge dissipation, a substantial residual potential is maintained over extended durations (Fig. S4). Importantly, within the time scale relevant to molecular self-assembly, the interfacial electric field remains sufficiently strong to drive molecular redistribution and adsorption, indicating functional stability of the polarization field during the assembly process. The progressive increase in surface potential reflects the continuous accumulation of triboelectric charges and the associated rise in surface charge density, which collectively strengthen the interfacial polarization field (Fig. S5). The enhanced field, in turn, facilitates ion migration and molecular adsorption at the solid-liquid interface, thereby improving the efficiency of self-assembly. For aqueous conditions, the surface potential evolution after immersion was also examined (Fig. S6). Although a faster decay is observed due to interfacial screening, a substantial residual potential is preserved, indicating that the interfacial field remains effective within the assembly time scale even in aqueous environments. Although electrostatic screening occurs in aqueous environments, the localized interfacial field remains sufficiently strong within the nanometer-scale region near the interface to govern ion redistribution and molecular adsorption. Based on the measured surface potential and the estimated surface charge density, the interfacial electric field can be reasonably expected to reach the order of 10^8-10^{10} V/m [42,64,65], consistent with reported values for contact electrification at solid-liquid interfaces. This field strength is sufficient to drive directional ion migration and molecular adsorption before complete screening occurs, thereby enabling the observed assembly process. Additional experiments using a positively triboelectric material (nylon) further confirm that the polarity of the triboelectrically induced polarization field can be reversibly programmed through material selection. However, efficient molecular assembly is found to depend strongly on the field strength, indicating that both the polarity and magnitude of the polarization field jointly govern interfacial adsorption and self-assembly. To corroborate the experimental potential distribution and to visualize the corresponding field geometry, we performed numerical simulations using COMSOL. The simulated surface potential after triboelectric agreed well with the measured values (Fig. 2B), and the computed electric-field distribution revealed a directional field pointing toward the FEP/Au surface (Fig. 2C), fully consistent with the proposed triboelectric-induced polarization mechanism. Together, these results establish that triboelectric-induced polarization produces a stable and spatially

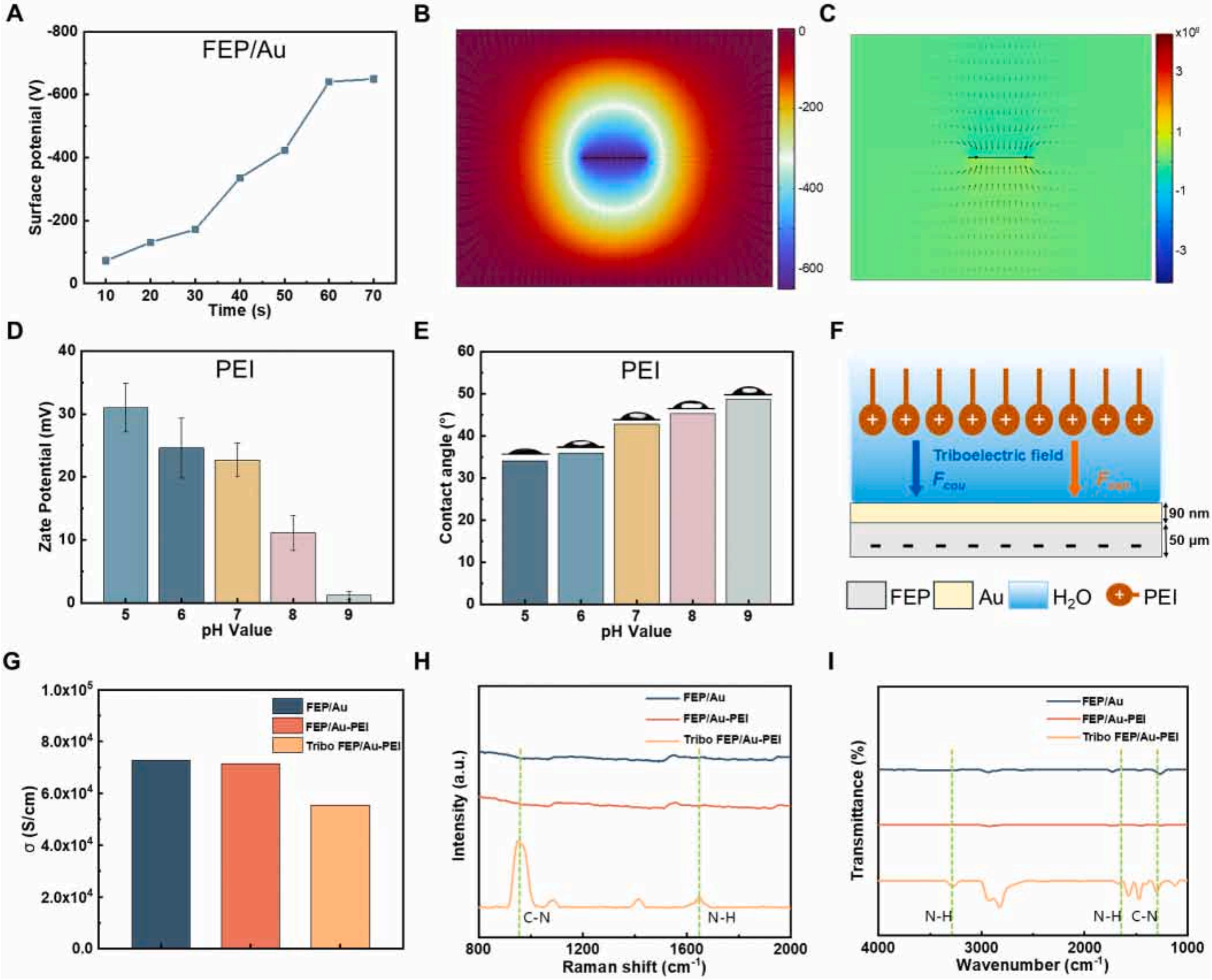

Fig. 2. Triboelectric-induced polarization and its role in directing molecular self-assembly. (A) Surface potential of Au measured after triboelectric between fur and FEP/Au for different durations. (B) Simulated surface potential distribution at the FEP/Au interface. (C) Simulated electric field distribution around the FEP/Au structure. (D) Zeta potential of PEI solutions versus pH. (E) Contact angle of PEI at different pH values. (F) Schematic illustration of forces governing triboelectric-induced polarization-driven molecular self-assembly. (G) Surface resistance of FEP/Au under different treatments. (H) Raman spectroscopic characterization of FEP/Au under different treatments. (I) FTIR spectroscopy characterization of FEP/Au under different treatments.

directed interfacial electric field capable of exerting long-range electrostatic forces on charged molecular species in solution. Because field-directed assembly depends not only on the field strength but also on the charge state of the building blocks, we next optimized the solution condition for PEI adsorption by tuning the degree of protonation of its amine groups. PEI contained abundant amine groups, whose degree of protonation varied significantly under different pH conditions. Adjusting the pH of the PEI solution was therefore critical for its self-assembly behavior. At low pH, most amine groups were protonated, generating more -NH_3^+ positive charges, which enhanced the polycationic character of the molecules and facilitated electrostatic adsorption onto negatively charged molecules or surfaces. However, when the pH was too low, excessive protonation led to strong intermolecular electrostatic repulsion, potentially causing aggregation or destabilization of the PEI layer. At high pH, partial deprotonation reduced the molecular charge density and weakened electrostatic adsorption. As shown in Fig. 2D, the zeta potential of PEI reached its maximum at pH 5, indicating the highest effective cationic character under our conditions and thus the most favorable electrostatic response to the triboelectric polarization field. Consistently, contact-angle measurements showed that PEI prepared at pH 5 yielded the lowest contact angle (Fig. 2E), suggesting improved wettability and stronger interfacial interactions. This reduced contact angle further promoted uniform adsorption of PEI onto the surface, thereby enhancing the efficiency and stability of the self-assembled layer.

Under these optimized conditions, PEI adsorption on triboelectric-induced polarization FEP/Au can be understood as a competition between long-range electrostatic attractions and short-range interfacial interactions (Fig. 2F). Charged molecules approaching the polarized surface were subjected to long-range Coulomb forces generated by the surface electric field, which guided their migration and adsorption. In addition, short-range van der Waals interactions contributed to the stabilization and dense packing of the adsorbed molecular layer. The combined effect of these forces controlled both the assembly kinetics and the structural uniformity of the self-assembled layer, highlighting the critical role of the balance between Coulomb and van der Waals interactions in triboelectric-induced polarization molecular self-assembly. Therefore, the assembly process can be understood as a field-initiated and interaction-stabilized mechanism, in which the triboelectric-induced polarization field governs the initiation and directionality of adsorption, while intermolecular interactions contribute to structural stabilization. The schematic illustration in Fig. 2F provides a qualitative summary of these interactions, as supported by the experimental results described above. A set of controls was then performed to directly demonstrate that PEI assembly requires triboelectric-induced polarization rather than simple immersion. The sheet resistance of the Au surface was measured using a four-probe method for pristine FEP/Au, for samples immersed in PEI and dried without polarization (FEP/Au-PEI), and for samples subjected to triboelectric-induced polarization prior to PEI immersion (Tribo FEP/Au-PEI) (Fig. 2G). The resistance of FEP/Au-PEI remained essentially unchanged compared with pristine FEP/Au, indicating that passive immersion does not produce a continuous PEI layer on Au. In contrast, Tribo FEP/Au-PEI exhibited a pronounced decrease in surface resistance, consistent with the formation of a more continuous interfacial coating after triboelectric-induced polarization assisted adsorption. In line with the hydrophilic nature of PEI, Tribo FEP/Au-PEI also showed a reduced contact angle relative to the non-triboelectric-induced polarization control (Fig. S7), further supporting successful interfacial modification. Finally, spectroscopic analyses provided chemical fingerprints of the assembled PEI layer. Raman spectra revealed FEP/Au and the FEP/Au-PEI exhibited no characteristic Raman peaks, indicating that no detectable PEI adsorption occurred on the Au surface under these conditions. In contrast, the Tribo FEP/Au-PEI sample showed distinct C-N and N-H Raman peaks after PEI immersion, which are consistent with the characteristic Raman fingerprints of PEI, Figs. 2 H and S8. FTIR measurements exhibited the same trend, with distinct PEI-associated absorption bands (notably N-H and C-N related features) appearing only after triboelectric-induced polarization assisted assembly while no such features were observed in the FEP/Au or FEP/Au-PEI samples (Figs. 2I and S9). These complementary electrical, wetting, and spectroscopic results collectively demonstrate that triboelectric-induced polarization generates a stable and directional interfacial field that is necessary to drive PEI adsorption and to form a chemically identifiable PEI layer on the FEP/Au surface. To further evaluate the material generality of the triboelectric-induced polarization strategy, we systematically investigated alternative triboelectric material pairings by varying both the dielectric substrate and the counter triboelectric material. When FEP was replaced with PTFE, a reduced surface potential was observed (Fig. S10), consistent with its weaker triboelectric performance. Correspondingly, Raman and FTIR results (Figs. S11 and S12) indicate a diminished PEI adsorption compared to the FEP-based system. Similarly, replacing fur with nylon as the counter triboelectric material resulted in a lower surface potential (Fig. S13) and weaker molecular assembly (Figs. S14 and S15). Despite these variations, molecular self-assembly was consistently observed across all tested material systems, indicating that the occurrence of assembly is not restricted to specific material combinations. Instead, the results reveal that the efficiency and extent of molecular assembly correlate with the strength of the triboelectric-induced polarization field. These findings suggest that triboelectric-induced polarization serves as a generalizable physical driving mechanism for molecular assembly, where the polarization field strength, rather than the specific material identity, acts as the key controlling parameter. To evaluate the role of ionic strength in the assembly process, NaCl was introduced at concentrations of 0.1 M and 1 M. Raman (Fig. S16) and FTIR (Fig. S17) spectra confirm that molecular assembly still occurs under these conditions, although the signal intensity is significantly reduced compared to the salt-free system. This reduction can be attributed to electrostatic screening in electrolyte solutions, where increasing ionic strength compresses the electrical double layer and shortens the effective range of the polarization field. Consequently, the ability of the field to drive ion redistribution from the bulk is diminished, leading to decreased assembly efficiency. Nevertheless, the persistence of assembly indicates that a strong localized interfacial field remains operative.

Having established that triboelectric-induced polarization is necessary to drive PEI adsorption, we next examined the structural morphology, spatial continuity, and chemical identity of the assembled PEI layer to elucidate its interfacial organization. Atomic force microscopy (AFM) was first employed to probe the surface topography of the Tribo FEP/Au-PEI sample at the nanoscale. As shown in Fig. 3A, the AFM height images reveal pronounced surface features compared with the relatively smooth FEP/Au substrate, indicating the formation of an adsorbed polymer layer. Brighter regions correspond to areas of increased thickness associated with PEI accumulation, while darker regions reflect thinner coverage or exposed substrate. To quantitatively analyze the thickness variation of the assembled layer, three-line profiles were extracted from the AFM topography, and the measurements were averaged. The analysis revealed that the height difference between the thicker and thinner regions of the self-assembled PEI layer was approximately 8.83 nm, indicating the formation of a multilayered PEI assembly on the FEP/Au surface rather than a sparse monolayer. This nanoscale thickness modulation suggests that triboelectric-induced polarization promotes not only initial molecular adsorption but also vertical buildup of PEI under electrostatic guidance. Complementary scanning electron microscopy (SEM) was used to investigate the surface morphology and microstructural features of the triboelectric-induced polarization assembled PEI layer. As shown in Fig. 3B, the Tribo FEP/Au-PEI surface exhibits a markedly different texture from bare FEP/Au, displaying heterogeneous contrast and clustered domains characteristic of polymer coverage. The surface exhibited clustered bright domains, which are indicative of localized PEI accumulation driven by triboelectric-induced polarization. These morphological features corroborate the structure observed in the AFM analysis. To verify the chemical composition of the assembled layer and to confirm the presence of PEI on the substrate, energy-dispersive X-ray spectroscopy (EDX) mapping was conducted in conjunction with SEM imaging. Since PEI is rich in carbon (C) and nitrogen (N) elements, elemental mapping focused on the spatial distribution of these two signatures. The EDX results revealed a clear co-localization of C and N signals with the bright regions observed in the SEM images. The uniform distribution of C and N across the analyzed area further validated that the surface was covered by an assembled PEI layer rather than contamination or substrate-related artifacts. The combined SEM and EDX analyses therefore provide strong evidence supporting the successful assembly of PEI on the FEP/Au surface.

To further resolve the chemical composition and bonding environment of the assembled layer, X-ray photoelectron spectroscopy (XPS) was conducted on FEP/Au-PEI (immersion only) and Tribo FEP/Au-PEI samples. As shown in Fig. 3C, the C 1 s spectrum of the immersion-only control FEP/Au-PEI displayed the characteristic C-C and C-F bonding signals originating from the FEP substrate and background carbon. In contrast, the Tribo FEP/Au-PEI sample exhibited an additional C-N peak, which is a signature bonding feature of PEI, confirming its presence on the surface. A minor C-O component was also observed, which may be attributed to slight oxidative modification of PEI. The N 1 s spectra (Fig. 3D) further supports this conclusion. In the FEP/Au-PEI sample, only a negligible N-H signal was detected, likely arising from trace contamination. However, the Tribo FEP/Au-PEI sample clearly exhibited multiple nitrogen-related peaks corresponding to N-H and -NH_2 groups, both of which are characteristic of PEI. The emergence and intensity of these nitrogen-related features unambiguously verify the chemical identity of the assembled layer. In the O 1 s spectra (Fig. 3E), both samples show weak signals primarily associated with adsorbed water, indicating that oxygen-containing species play a minimal role in the interfacial chemistry of the PEI layer. Taken together, AFM reveals the nanoscale thickness and multilayer nature of the PEI coating, SEM/EDX confirms its lateral continuity and elemental composition, and XPS further verified the emergence of characteristic C-N, N-H, and -NH_2 bonding signals exclusive to PEI. These complementary characterizations collectively demonstrate that triboelectric-induced polarization drives the formation of a continuous, chemically distinct PEI layer on the

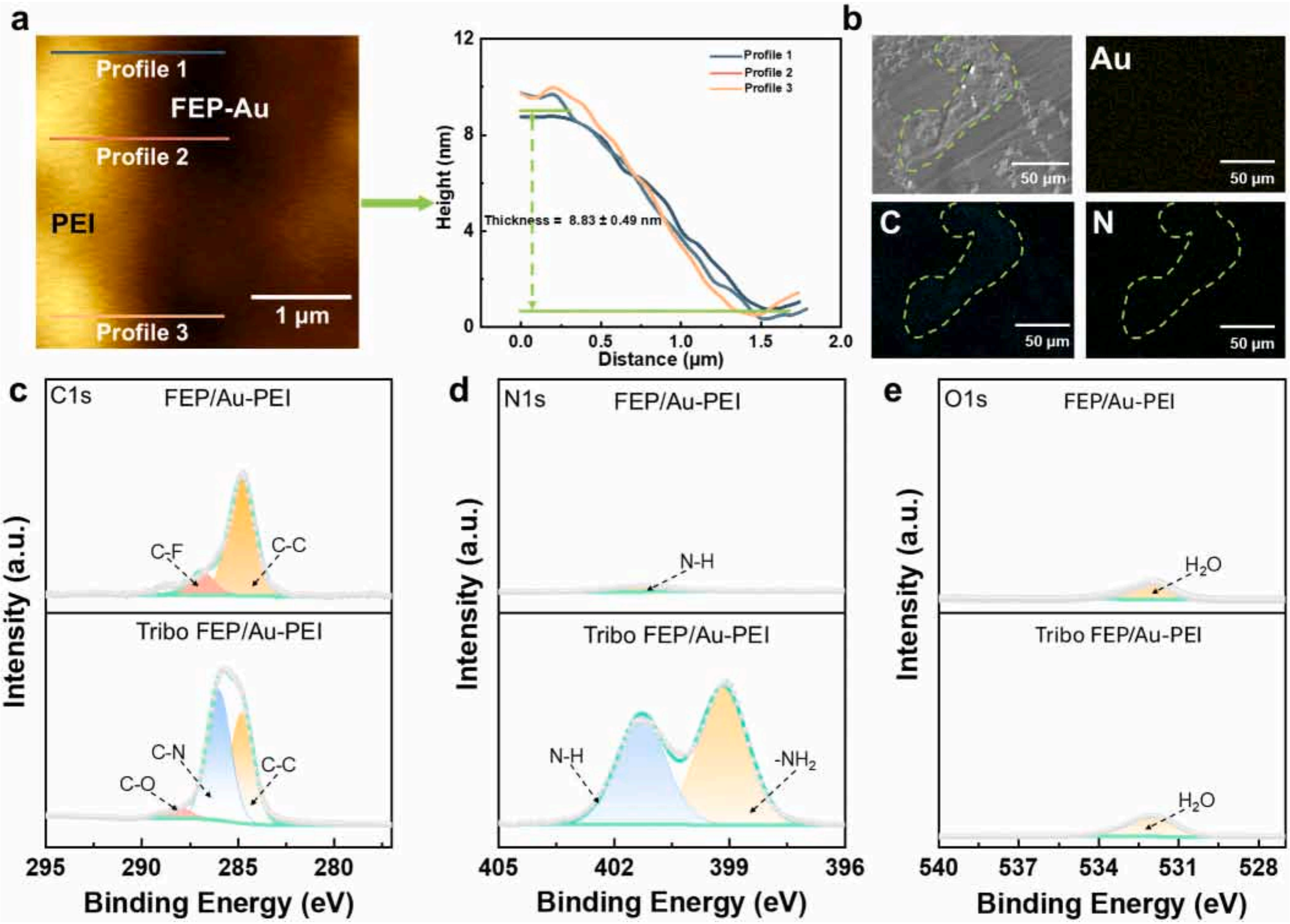

Fig. 3. Characterizations reveal interfacial organization of triboelectric-induced polarization-driven FEP/Au-PEI. (A) AFM height images and line profiles show height variations indicative of PEI self-assembly on Tribo FEP/Au-PEI. (B) SEM morphology images and EDX elemental maps of Tribo FEP/Au-PEI. (C) XPS C 1 s spectra of FEP/Au-PEI and Tribo FEP/Au-PEI. (D) XPS N 1 s spectra of FEP/Au-PEI and Tribo FEP/Au-PEI. (E) XPS O 1 s spectra of FEP/Au-PEI and Tribo FEP/Au-PEI.

FEP/Au surface. Importantly, the assembled structure is not the result of nonspecific adsorption but arises from field-directed molecular organization enabled by mechanically generated interfacial polarization.

2.3. Triboelectric-induced polarization-enabled PEI/ALG LbL assembly and underwater self-cleaning

With the establishment of a well-defined PEI layer assembled through triboelectric-induced polarization, the FEP/Au surface becomes positively charged and chemically activated, providing a suitable platform for subsequent LbL molecular assembly. We therefore proceeded to construct a second layer by depositing ALG onto Tribo FEP/Au-PEI, aiming to form a hierarchical PEI/ALG multilayer architecture. Because the adsorption of ALG is governed by its ionization state, we first evaluated the solution charge characteristics of ALG by zeta-potential measurements as a function of pH (Fig. S18). At low pH, carboxyl groups remain largely protonated (-COOH), reducing the net negative charge and promoting polymer aggregation/precipitation; upon increasing pH, progressive deprotonation to -COO$^-$ enhances the anionic character of ALG. At higher pH values, the zeta potential slightly decreased, which may have been attributed to changes in ionic strength partially shielding surface charges. In our system, ALG exhibited the highest magnitude of negative zeta potential at pH 7, indicating an optimal charge state for electrostatic coupling with the PEI-coated surface. Accordingly, Tribo FEP/Au-PEI samples were immersed in ALG solution at pH 7, followed by rinsing and drying to yield Tribo FEP/Au-PEI-ALG. Multiple complementary measurements confirm successful ALG deposition and the formation of a stable PEI/ALG multilayer. First, compared with the original FEP/Au substrate, the Tribo FEP/Au-PEI-ALG surface exhibits a markedly reduced water contact angle, indicating successful assembly of a hydrophilic ALG polysaccharide overlayer on the Tribo FEP/Au-PEI surface (Fig. S19). Subsequently, Raman spectroscopy was performed to further confirm the presence of ALG. Characteristic Raman peaks corresponding to the C-O-C and the C═O, which are typical of alginate, were clearly detected on the Tribo FEP/Au-PEI-ALG sample (Fig. S20). Following the Raman analysis, FTIR measurements were conducted, and the spectra similarly revealed absorptions associated with C-O-C and C═O groups (Fig. S21). These consistent spectroscopic results verified the existence of ALG on the Tribo FEP/Au-PEI surface and provided a solid basis for subsequent functional characterization. To further clarify the underlying mechanism and distinguish the role of the polarization field from intrinsic intermolecular interactions, it is important to note that the assembly process in the PEI/ALG system may involve multiple noncovalent interactions, including electrostatic attraction and hydrogen bonding. As shown in Fig. 2G-I, when the FEP/Au substrate is directly immersed in PEI solution without triboelectric-induced polarization, no detectable PEI adsorption is observed, as evidenced by the unchanged surface resistance and the absence of characteristic Raman and FTIR signals. In contrast, after the introduction of triboelectric-induced polarization, a well-defined PEI layer is formed on the substrate. These results indicate that intrinsic interactions alone-including hydrogen bonding and weak electrostatic adsorption are insufficient to initiate molecular assembly on the unmodified surface. Instead, the triboelectric-induced polarization-generated interfacial electric field plays a decisive role in triggering the initial adsorption process. For the subsequent LbL assembly of ALG onto the PEI-coated surface, both electrostatic interactions and hydrogen bonding are expected to coexist and contribute to the stabilization of the multilayer structure. However, the initiation, spatial localization, and directionality of the assembly are governed by the triboelectric-induced polarization field, which establishes the initial charged template and drives the sequential adsorption process. Therefore, while intrinsic intermolecular interactions contribute to structural stabilization, the triboelectric-induced polarization field serves as the primary driving force that initiates and directs the assembly process.

To resolve the interfacial chemical composition and to verify the coexistence of PEI and ALG within the multilayer, we performed X-ray photoelectron spectroscopy (XPS). As shown in Fig. 4A, the C 1 s spectrum displayed multiple well-defined components. The peak centered around the binding energy associated with C-N confirmed the contribution of the PEI layer, consistent with the amine-rich structure of PEI. In addition, two prominent peaks corresponding to C-O and C=O were clearly observed, which are characteristic of the saccharide backbone of ALG. The emergence and significant intensity of these oxygen-containing carbon species indicated the formation of an ALG overlayer on top of the PEI-modified surface. Compared with the Tribo FEP/Au-PEI sample, the increased C-O and C=O signals provided direct chemical evidence of the successful adsorption of ALG. The N 1 s spectrum (Fig. 4B) further supported these findings. Clear peaks corresponding to N-H and $-NH_2$ groups, both originating from PEI, were observed on the

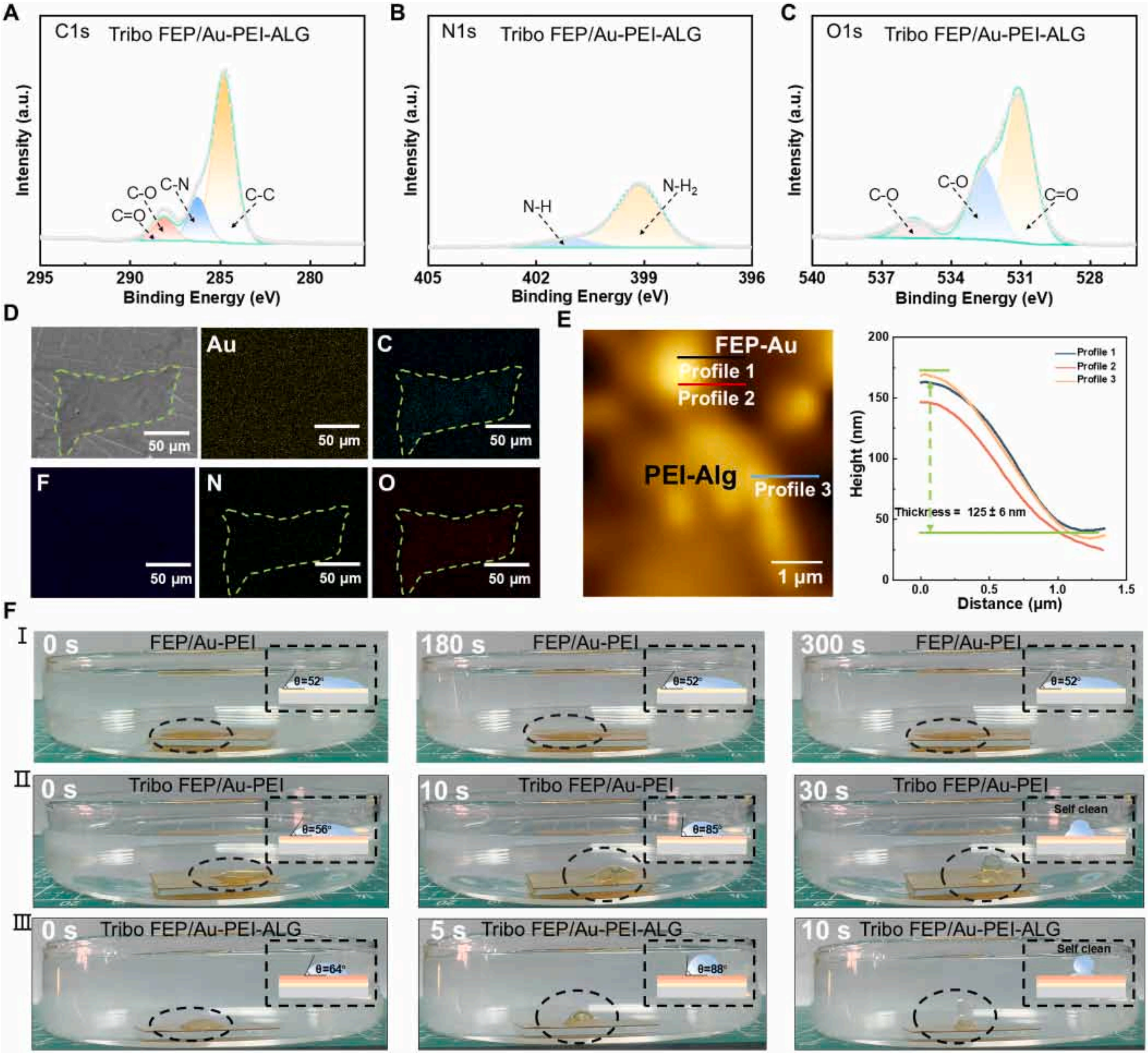

Fig. 4. Self-assembly characterization and self-cleaning application of triboelectric-induced polarization Tribo FEP/Au-PEI-ALG. (A) XPS C 1 s spectra of Tribo FEP/Au-PEI-ALG. (B) XPS N 1 s spectra of Tribo FEP/Au-PEI-ALG. (C) XPS O 1 s spectra of Tribo FEP/Au-PEI-ALG. (D) SEM morphology images and EDX elemental maps of Tribo FEP/Au-PEI-ALG. (E) AFM height images and line profiles show height variations indicative of PEI-ALG self-assembly on Tribo FEP/Au-PEI-ALG. (F) Underwater oil adhesion and self-cleaning tests comparing FEP/Au under different treatment conditions.

Tribo FEP/Au-PEI-ALG sample. The presence of these distinct nitrogen peaks indicated that the underlying PEI layer was still retained after ALG assembly, suggesting that the adsorption process did not disrupt the amine functionalities but instead formed an additional ALG on top of it. The relative intensity of the nitrogen peaks also reflected the expected attenuation due to the presence of the ALG overlayer, further supporting the formation of a multilayered structure. The O 1 s spectrum shown in Fig. 4C exhibited two primary components attributable to O-C and O=C species, which are characteristic of the carboxylate and hydroxyl groups distributed along the alginate polymer chains. Compared with the background oxygen signal of the Tribo FEP/Au-PEI surface, the significantly enhanced O 1 s components provided additional confirmation of the presence of ALG. Together, these XPS results confirm a chemically stratified PEI/ALG architecture rather than nonspecific adsorption of a single component. Additional supporting characterizations XRD indicate that all samples showed characteristic peaks of FEP and Au, indicating that the structure of the substrate was retained (Fig. S22). However, the peak intensities gradually decreased from FEP/Au-PEI to Tribo FEP/Au-PEI and Tribo FEP/Au-PEI-ALG. This attenuation can be attributed to the successive deposition of PEI and ALG layers, which partially shielded the substrate from the X-ray beam. UV–vis absorption spectra of Tribo FEP/Au-PEI and Tribo FEP/Au-PEI-ALG were further measured (Fig. S23). In the ultraviolet region, the absorption intensity of Tribo FEP/Au-PEI-ALG was lower than that of Tribo FEP/Au-PEI, which can be attributed to the formation of an ALG overlayer partially covering the underlying PEI. This decrease in absorption provides additional evidence for the successful adsorption of ALG onto the PEI-modified surface, consistent with the structural and chemical characterizations described above. We next examined the morphology and thickness of the resulting PEI/ALG multilayer. SEM images reveal a continuous polymeric coating with distinct surface texture relative to the bare substrate (Fig. 4D). To further confirm the composition of these layers, EDX mapping was performed across the surface. The analysis detected C, contributed by both PEI and ALG, N, originating from the underlying PEI layer, and O, predominantly associated with the ALG coating. Spatial mapping showed that N was distributed throughout the PEI layer but appeared relatively attenuated in regions covered by ALG, indicating partial shielding of the PEI signal by the polysaccharide overlayer. O was uniformly distributed over the surface, consistent with a continuous ALG layer. These results not only confirmed the successful deposition of ALG onto the PEI-modified surface but also supported the formation of a well-defined multilayered structure. AFM topography (Fig. 4E) provides quantitative thickness information, revealing an average multilayer thickness of ~125 nm from line-profile analysis, indicating substantial vertical build-up through sequential adsorption. Importantly, electrochemical measurements (potentiostatic response and cyclic voltammetry) show no significant perturbation relative to controls (Figs. S24 and S25), suggesting that the polymer assembly predominantly modifies interfacial wetting/adhesion behavior without introducing pronounced electrochemical side reactions on the Au substrate under the tested conditions. Finally, given that hydrophilic surfaces can repel oils in aqueous environments and facilitate spontaneous contaminant release, we evaluated whether the polysaccharide-rich ALG coating confers practical antifouling and self-cleaning behavior to the modified substrate. Underwater oil-adhesion tests show a clear progression from strong oil wetting on FEP/Au-PEI to weakened adhesion on Tribo FEP/Au-PEI and the most pronounced oil repellence on Tribo FEP/Au-PEI-ALG (Fig. 4F). Specifically, the immersion-only PEI sample exhibits persistent oil spreading and stable adhesion over minutes (Fig. 4F I), whereas Tribo FEP/Au-PEI displays time-dependent contraction of the oil droplet followed by spontaneous detachment (~30 s; Fig. 4F II). Remarkably, Tribo FEP/Au-PEI-ALG shows the largest initial underwater oil contact angle and the fastest detachment, with complete release occurring within ~10 s (Fig. 4F III). To evaluate the robustness of the self-cleaning performance, a range of oil phases and chemically complex aqueous environments were systematically investigated. Both olive oil and liquid paraffin undergo spontaneous detachment, albeit with distinct detachment dynamics (Fig. S26). In high-ionic-strength electrolytes containing NaCl, $CaCl_2$, and $MgCl_2$, the detachment kinetics are slowed as a result of enhanced electrostatic screening; nevertheless, the self-cleaning functionality remains well preserved (Fig. S27). The self-cleaning demonstration is presented as a qualitative illustration of surface functionality under the studied conditions. Fig. 4F provides a schematic illustration of the interfacial processes underlying oil detachment. This accelerated de-oiling behavior is consistent with the formation of a highly hydrophilic outer layer that supports a stable hydration layer and reduces interfacial oil adhesion. Collectively, these results demonstrate that triboelectric-induced polarization not only enables power-free LbL molecular assembly but also provides a route to functional underwater interfaces with rapid self-cleaning capability.

In principle, spatially patterned polarization fields could be achieved through controlled triboelectrification, as the underlying mechanism is governed by spatially distributed surface charges. By engineering contact geometry, pressure distribution, or sliding trajectories during the triboelectric process, localized variations in charge density can be introduced, leading to spatially resolved interfacial electric fields. Such patterned fields could enable selective adsorption of charged molecular species, thereby guiding spatially controlled molecular assembly at solid-liquid interfaces. Furthermore, by dynamically tuning triboelectric conditions during sequential assembly steps, it may be possible to construct hierarchical multilayer structures with spatially varying composition and functionality. These considerations suggest a promising route toward programmable interfacial assembly and the development of patterned functional materials.

3. Conclusion

In summary, we demonstrate that triboelectric-induced polarization can serve as a mechanically generated, bias-free interfacial electric field to direct molecular self-assembly at solid-liquid interfaces. A stable and directional polarization field enables the LbL assembly of PEI/ALG multilayers without surface functionalization or external electrical input, as confirmed by systematic characterizations. The assembly process is governed by the polarization field, which directs molecular migration and interfacial organization. The resulting interface exhibits robust underwater self-cleaning behavior across different oil phases and complex aqueous environments, highlighting the functional relevance of this approach. These results establish triboelectric-induced polarization as a generalizable physical driving mechanism, where the field strength, rather than specific material identity, acts as the key controlling parameter. Several limitations remain. The uniformity of the assembled layers may be affected by spatial heterogeneity of the polarization field, while precise control is limited by the stochastic nature of contact electrification. In addition, field attenuation in aqueous environments and environmental factors such as humidity and ionic strength may influence reproducibility and scalability. Future work should focus on improving field controllability, developing patterned polarization strategies, and enabling more precise and programmable molecular assembly.

4. Experimental section

4.1. Materials

The metal charge-collecting layer on the dielectric substrate surface was sputtered by the magnetron sputtering deposition system (Discovery 635, Denton Vacuum, America). The sputtering power used for this process was 50 W. The sputtering method was set to DC sputtering. The rotational speed during sputtering was kept at 50 r/min. The DI water with a resistivity of 18.2 MΩ·cm used here was produced by a deionizer (HHitech, China). The 50 μm-thick Fluorinated Ethylene Propylene (FEP) film (industrial grade). Polyetherimide (PEI), Aladdin, MW

70,000, 50% aqueous solution. Sodium alginate, Macklin, reagent grade, 90%.

4.2. Characterization and measurement

The surface morphologies of Tribo FEP/Au-PEI and Tribo FEP/Au-PEI-ALG membranes were examined using a field-emission scanning electron microscope (FEI/Nova NanoSEM450). Measurements were conducted under a N2 atmosphere: morphological imaging was performed at an accelerating voltage of 5 kV, while elemental analysis was carried out using an energy-dispersive X-ray spectroscopy (EDS) system at 20 kV with a beam current of 10 nA. Samples were pre-coated with a gold–palladium alloy for 120 s to enhance conductivity. Membrane pore structures were analyzed by X-ray diffraction (XRD) using a Bruker D8 ADVANCE diffractometer with Cu Kα radiation ($\lambda = 1.54$ Å). Prior to measurement, sample surfaces were cleaned and flattened; scans were conducted at 5–45° (2θ) at room temperature, and the interplanar spacing (d) was calculated using Bragg's law ($2d \sin\theta = n\lambda$, where n is an integer, λ is the X-ray wavelength, and θ is the diffraction angle). Surface morphology and thickness of membranes were further characterized by atomic force microscopy (Asylum Research, Oxford Instruments). Zeta potential measurements were performed at 25°C using a BeNano Zeta analyzer (Dandong Betters). Chemical structures were investigated by Fourier-transform infrared spectroscopy (FTIR, Bruker VERTEX80v) and X-ray photoelectron spectroscopy (XPS, Thermo Fisher K-Alpha, Al Kα source, 1486.6 eV, 10 mA, 15 kV). Surface wettability was evaluated by measuring the water contact angle, conducted at room temperature using a contact angle goniometer (DSA100, LAUDA Scientific, Germany). All electrochemical measurements were carried out using a Multi Auto-lab M204 electrochemical workstation.

4.3. Simulations methods

In the COMSOL Multiphysics software, the Electrostatics Module was employed to conduct an electrostatic field simulation of the charged FEP-Au composite sample. Considering that the Au layer used in the experiment has a thickness of merely 90 nm and, as a good conductor, inherently satisfies the equipotential property, the Au layer was not designed as a solid domain. Instead, it was directly applied to the contact surface between the FEP film and the Au layer in the form of a terminal boundary condition under the Electrostatics Module. Eventually, the model was simplified into two geometric structures: one is the FEP film, and the other is the air domain that encloses the FEP film.

The material parameters were set based on the physical properties of the materials used in the experiment: the relative permittivity of FEP was set to 2.1, and that of air was set to 1.0. In terms of boundary conditions, all boundaries of the air domain were set to ground ($V = 0$) to simulate an infinite far-field environment; the terminal voltage corresponding to the Au layer was set to $V = V_0$, which refers to the electrostatic potential of the Au surface measured by a surface potentiometer in the experiment. Meanwhile, the parametric sweep of the terminal voltage was utilized to reproduce different charged states of the sample.

The simulation was solved under steady-state conditions to calculate the potential and electric field distributions around the sample. During postprocessing, the potential distribution and electric field distribution of the FEP film and the air domain, as well as the electric field intensity on the Au surface, were extracted. The variation patterns of various physical quantities under different V_0 were analyzed quantitatively, providing reliable data support for explaining the mechanism of experimental phenomena.

Authors contribution

D.W. and Z.L.W. proposed the idea and the project. D.W. designed all the experiments and supervised the whole project. Y.W. carried out the experiments in this paper. B.B.S. and J.J.S provided support for the Simulations. Y.W. and X.L. analyzed the corresponding data. All the authors discussed the results and commented on the manuscript. D.W., Y.W. and X.L. wrote this paper.

CRediT authorship contribution statement

Jiajia Shao: Validation, Supervision. **Lixue Yang:** Validation, Formal analysis. **Di Wei:** Writing – review & editing, Supervision, Resources, Project administration, Methodology, Funding acquisition, Formal analysis, Data curation, Conceptualization. **Zhong Lin Wang:** Supervision, Resources, Funding acquisition. **Yu Wei:** Writing – original draft, Validation, Methodology, Investigation, Formal analysis, Data curation, Conceptualization. **Bobo Sun:** Validation, Data curation. **Xiang Li:** Writing – review & editing, Supervision, Funding acquisition, Data curation, Conceptualization.

Declaration of Competing Interest

The authors declare that they have no known competing financial interests or personal relationships that could have appeared to influence them.

Acknowledgements

This work is supported by the National Natural Science Foundation of China (Grant No. 22479016 D.W.) and China Postdoctoral Science Foundation (Certificate Number: 2025M781041 X.L.).

Appendix A. Supporting information

Supplementary data associated with this article can be found in the online version at doi:10.1016/j.nanoen.2026.111991.

Data availability

Data will be made available on request.

References

[1] D. Pochan, O. Scherman, Introduction: molecular self-assembly, Chem. Rev. 121 (2021) 13699–13700, https://doi.org/10.1021/acs.chemrev.1c00884.

[2] Q. Song, Z. Cheng, M. Kariuki, S.C.L. Hall, S.K. Hill, J.Y. Rho, S. Perrier, Molecular self-assembly and supramolecular chemistry of cyclic peptides, Chem. Rev. 121 (2021) 13936–13995, https://doi.org/10.1021/acs.chemrev.0c01291.

[3] D.P. August, R.A.W. Dryfe, S.J. Haigh, P.R.C. Kent, D.A. Leigh, J.-F. Lemonnier, Z. Li, C.A. Muryn, L.I. Palmer, Y. Song, G.F.S. Whitehead, R.J. Young, Self-assembly of a layered two-dimensional molecularly woven fabric, Nature 588 (2020) 429–435, https://doi.org/10.1038/s41586-020-3019-9.

[4] N.M. Lissin, S.Y. Venyaminov, A.S. Girshovich, Mg–ATP)-dependent self-assembly of molecular chaperone GroEL, Nature 348 (1990) 339–342, https://doi.org/10.1038/348339a0.

[5] F. Beuerle, Unexplored territory for self-assembly, Nature 540 (2016) 529–530, https://doi.org/10.1038/540529a.

[6] M. Fujita, F. Ibukuro, H. Hagihara, K. Ogura, Quantitative self-assembly of a [2] catenane from two preformed molecular rings, Nature 367 (1994) 720–723, https://doi.org/10.1038/367720a0.

[7] Z. Li, Q. Fan, Y. Yin, Colloidal self-assembly approaches to smart nanostructured materials, Chem. Rev. 122 (2022) 4976–5067, https://doi.org/10.1021/acs.chemrev.1c00482.

[8] W. Chang, J. Kim, M. Kim, M.W. Lee, C.H. Lim, G. Kim, S. Hwang, J. Chang, Y. H. Min, K. Jeon, S. Kim, Y.-H. Choi, J.S. Lee, Concurrent self-assembly of RGB microLEDs for next-generation displays, Nature 617 (2023) 287–291, https://doi.org/10.1038/s41586-023-05889-w.

[9] A. McMullen, M. Muñoz Basagoiti, Z. Zeravcic, J. Brujic, Self-assembly of emulsion droplets through programmable folding, Nature 610 (2022) 502–506, https://doi.org/10.1038/s41586-022-05198-8.

[10] M. Du, K. Zhou, R. Yu, Y. Zhai, G. Chen, Q. Wang, Noncovalent self-assembly of protein crystals with tunable structures, Nano Lett. 21 (2021) 1749–1757, https://doi.org/10.1021/acs.nanolett.0c04587.

[11] G. Mariani, D. Moldenhauer, R. Schweins, F. Gröhn, Elucidating electrostatic self-assembly: molecular parameters as key to thermodynamics and nanoparticle shape, J. Am. Chem. Soc. 138 (2016) 1280–1293, https://doi.org/10.1021/jacs.5b11497.

[12] L. Taussig, M. Ghasemi, S. Han, A.L. Kwansa, R. Li, S.T. Keene, N. Woodward, Y. G. Yingling, G.G. Malliaras, E.D. Gomez, A. Amassian, Electrostatic self-assembly

yields a structurally stabilized PEDOT:PSS with efficient mixed transport and high-performance OECTs, Matter 7 (2024) 1071–1091, https://doi.org/10.1016/j.matt.2023.12.021.

[13] A.S. Parmar, J.K. James, D.R. Grisham, D.H. Pike, V. Nanda, Dissecting electrostatic contributions to folding and self-assembly using designed multicomponent peptide systems, J. Am. Chem. Soc. 138 (2016) 4362–4367, https://doi.org/10.1021/jacs.5b10304.

[14] Q. Liu, H. Yu, Q. Zhang, D. Wang, X. Wang, Temperature-responsive self-assembly of single polyoxometalates clusters driven by hydrogen bonds, Adv. Funct. Mater. 31 (2021) 2103561, https://doi.org/10.1002/adfm.202103561.

[15] G.-L. Li, Z. Zhuo, B. Wang, X.-L. Cao, H.-F. Su, W. Wang, Y.-G. Huang, M. Hong, Constructing π-stacked supramolecular cage based hierarchical self-assemblies via π···π stacking and hydrogen bonding, J. Am. Chem. Soc. 143 (2021) 10920–10929, https://doi.org/10.1021/jacs.1c01161.

[16] J. Li, L. Kan, J. Li, Y. Liu, M. Eddaoudi, Quest for zeolite-like supramolecular assemblies: self-assembly of metal–organic squares via directed hydrogen bonding, Angew. Chem. Int. Ed. 59 (2020) 19659–19662, https://doi.org/10.1002/anie.202006978.

[17] B. Akram, B. Ni, X. Wang, Van der Waals integrated hybrid POM-zirconia flexible belt-like superstructures, Adv. Mater. 32 (2020) 1906794, https://doi.org/10.1002/adma.201906794.

[18] Z. Zhang, Y. Chen, P. Shen, J. Chen, S. Wang, B. Wang, S. Ma, B. Lyu, X. Zhou, S. Lou, Z. Wu, Y. Xie, C. Zhang, L. Wang, K. Xu, H. Li, G. Wang, K. Watanabe, T. Taniguchi, D. Qian, J. Jia, Q. Liang, X. Wang, W. Yang, G. Zhang, C. Jin, W. Ouyang, Z. Shi, Homochiral carbon nanotube van der Waals crystals, Science 387 (2025) 1310–1316, https://doi.org/10.1126/science.adu1756.

[19] B. Olenyuk, J.A. Whiteford, A. Fechtenkötter, P.J. Stang, Self-assembly of nanoscale cuboctahedra by coordination chemistry, Nature 398 (1999) 796–799, https://doi.org/10.1038/19740.

[20] R. Adam, M. Mon, R. Greco, L.H.G. Kalinke, A. Vidal-Moya, A. Fernandez, R.E. P. Winpenny, A. Doménech-Carbó, A. Leyva-Pérez, D. Armentano, E. Pardo, J. Ferrando-Soria, Self-assembly of catalytically active supramolecular coordination compounds within metal–organic frameworks, J. Am. Chem. Soc. 141 (2019) 10350–10360, https://doi.org/10.1021/jacs.9b03914.

[21] J. Landman, S. Ouhajji, S. Prévost, T. Narayanan, J. Groenewold, A.P. Philipse, W. K. Kegel, A.V. Petukhov, Inward growth by nucleation: Multiscale self-assembly of ordered membranes, Sci.Adv. 4 eaat1817. https://doi.org/10.1126/sciadv.aat1817.

[22] A. Sellinger, P.M. Weiss, A. Nguyen, Y. Lu, R.A. Assink, W. Gong, C.J. Brinker, Continuous self-assembly of organic–inorganic nanocomposite coatings that mimic nacre, Nature 394 (1998) 256–260, https://doi.org/10.1038/28354.

[23] Y. Ma, C.-F. Xu, X.-R. Mao, Y. Wu, J. Yang, L.-P. Xu, M.-P. Zhuo, H. Lin, S. Zhuo, X.-D. Wang, Oriented self-assembly of hierarchical branch organic crystals for asymmetric photonics, J. Am. Chem. Soc. 145 (2023) 9285–9291, https://doi.org/10.1021/jacs.3c02061.

[24] H.-Y. Lee, S.H.R. Shin, A.M. Drews, A.M. Chirsan, S.A. Lewis, K.J.M. Bishop, Self-assembly of nanoparticle amphiphiles with adaptive surface chemistry, ACS Nano 8 (2014) 9979–9987, https://doi.org/10.1021/nn504734v.

[25] Q. Tao, S. Huang, X. Li, X.-F. Chu, X. Lu, D. Wang, Counterion-dictated self-cleaning behavior of polycation coating upon water action: macroscopic dissection of hydration of anions, Angew. Chem. Int. Ed. 59 (2020) 14466–14472, https://doi.org/10.1002/anie.202002819.

[26] S. Huang, D. Wang, A simple nanocellulose coating for self-cleaning upon water action: molecular design of stable surface hydrophilicity, Angew. Chem. Int. Ed. 56 (2017) 9053–9057, https://doi.org/10.1002/anie.201703913.

[27] D.E. Chafai, V. Sulimenko, D. Havelka, L. Kubínová, P. Dráber, M. Cifra, Reversible and irreversible modulation of tubulin self-assembly by intense nanosecond pulsed electric fields, Adv. Mater. 31 (2019) 1903636, https://doi.org/10.1002/adma.201903636.

[28] G. Camacho, J. de Vicente, Template-free ultrafast directed self-assembly using biaxial toggled magnetic fields, ACS Nano 19 (2025) 28873–28887, https://doi.org/10.1021/acsnano.5c09450.

[29] D. Alessi, L. Morgan, E. Pelorosso, C. Graiff, P. Pinter, A. Aliprandi, Redox-driven photoselective self-assembly, Nat. Commun. 16 (2025) 4316, https://doi.org/10.1038/s41467-025-58890-4.

[30] X. Liu, M. Wei, Q. Wang, Y. Tian, J. Han, H. Gu, H. Ding, Q. Chen, K. Zhou, Z. Gu, Capillary-force-driven self-assembly of 4D-printed microstructures, Adv. Mater. 33 (2021) 2100332, https://doi.org/10.1002/adma.202100332.

[31] L. Wågberg, J. Erlandsson, The use of layer-by-layer self-assembly and nanocellulose to prepare advanced functional materials, Adv. Mater. 33 (2021) 2001474, https://doi.org/10.1002/adma.202001474.

[32] W. Ran, A. Walz, K. Stoiber, P. Knecht, H. Xu, A.C. Papageorgiou, A. Huettig, D. Cortizo-Lacalle, J.P. Mora-Fuentes, A. Mateo-Alonso, H. Schlichting, J. Reichert, J.V. Barth, Depositing molecular graphene nanoribbons on Ag(111) by electrospray controlled ion beam deposition: self-assembly and on-surface transformations, Angew. Chem. Int. Ed. 61 (2022) e202111816, https://doi.org/10.1002/anie.202111816.

[33] H. Gan, H. Liu, Y. Li, Q. Zhao, Y. Li, S. Wang, T. Jiu, N. Wang, X. He, D. Yu, D. Zhu, Fabrication of polydiacetylene nanowires by associated self-polymerization and self-assembly processes for efficient field emission properties, J. Am. Chem. Soc. 127 (2005) 12452–12453, https://doi.org/10.1021/ja053352k.

[34] B.D. Terris, J.E. Stern, D. Rugar, H.J. Mamin, Contact electrification using force microscopy, Phys. Rev. Lett. 63 (1989) 2669–2672, https://doi.org/10.1103/PhysRevLett.63.2669.

[35] J.C. Sobarzo, F. Pertl, D.M. Balazs, T. Costanzo, M. Sauer, A. Foelske, M. Ostermann, C.M. Pichler, Y. Wang, Y. Nagata, M. Bonn, S. Waitukaitis, Spontaneous ordering of identical materials into a triboelectric series, Nature 638 (2025) 664–669, https://doi.org/10.1038/s41586-024-08530-6.

[36] Y. Wei, X. Li, Y. Gu, L. Ding, X. Gao, Z. Zhang, C. Kvarnström, J. Bobacka, A. Ivaska, Z.-Q. Tian, Z.L. Wang, D. Wei, Probing electrical double layer via triboelectric charge transfer, Nat. Commun. (2025), https://doi.org/10.1038/s41467-025-67094-9.

[37] Y. Du, Z.L. Wang, D. Chu, G. Amaratunga, D. Wei, Iontronics for adaptive and flexible pressure sensing, Iontronics 2 (2026) 13, https://doi.org/10.20517/iontronics.2026.13.

[38] L. Shi, R.A. LaCour, N. Qian, J.P. Heindel, X. Lang, R. Zhao, T. Head-Gordon, W. Min, Water structure and electric fields at the interface of oil droplets, Nature 640 (2025) 87–93, https://doi.org/10.1038/s41586-025-08702-y.

[39] Y. Wei, X. Li, Z. Yang, J. Shao, Z.L. Wang, D. Wei, Contact electrification at the solid–liquid transition interface, Mater. Today 74 (2024) 2–11, https://doi.org/10.1016/j.mattod.2024.03.013.

[40] H. Hao, I. Leven, T. Head-Gordon, Can electric fields drive chemistry for an aqueous microdroplet? Nat. Commun. 13 (2022) 280, https://doi.org/10.1038/s41467-021-27941-x.

[41] S.M. Kathmann, I.F.W. Kuo, C.J. Mundy, Electronic effects on the surface potential at the vapor−liquid interface of water, J. Am. Chem. Soc. 130 (2008) 16556–16561, https://doi.org/10.1021/ja802851w.

[42] S. Li, Z.L. Wang, D. Wei, Hidden interfacial electric fields in chemistry: contact electrification and beyond, Chem. Soc. Rev. (2026), https://doi.org/10.1039/D5CS01066G.

[43] C. Ye, D. Liu, Y. Gao, F. Liu, H. Xu, T. Jiang, Z.L. Wang, Electrostatic breakdown at liquid-solid-gas triple-phase interfaces owing to contact electrification, Matter 8 (2025) 102007, https://doi.org/10.1016/j.matt.2025.102007.

[44] N. Wang, H. Feng, J. Yang, J.H. Pan, E. Ye, W. Jiang, Y.-W. Zhang, Z. Wang, X. J. Loh, Z. Li, Boosted contact-electro-catalytic CO2 to methanol enabled by a built-in electric field design, Nano Energy 152 (2026) 111883, https://doi.org/10.1016/j.nanoen.2026.111883.

[45] N. Wang, H. Feng, J. Yang, J. Zheng, Y.-W. Zhang, N. Hadjichristidis, Z. Li, In situ high selectivity contact-electroreduction of CO2 to methanol using an imine-mediated metal-free vitrimer catalyst, Angew. Chem. 137 (2025) e202500222, https://doi.org/10.1002/ange.202500222.

[46] X. Li, T. Cheng, Z.L. Wang, D. Wei, Neuromimetic circuits enabled by dynamic regulation of the electrical double layer, npj Flex. Electron. 9 (2025) 66, https://doi.org/10.1038/s41528-025-00450-3.

[47] X. Wang, A.P. Ivanov, J.B. Edel, Biocompatible biphasic iontronics enable neuron-like ionic signal transmission, Research 7 (2024) 0294, https://doi.org/10.34133/research.0294.

[48] P. Zhuang, L. Chen, Y. Zhang, W. Yang, Y. Chen, L. Wu, L. Xiang, Z. Wang, J. M. Rosenholm, G. Zuo, T. Ye, H. Zhang, W. Cui, Solid-liquid interface lubricating hydrogels for tendon-bone healing, Research 8 (2025) 0924, https://doi.org/10.34133/research.0924.

[49] J. Yin, P. Jia, Z. Ren, Q. Zhang, W. Lu, Q. Yao, M. Deng, X. Zhou, Y. Gao, N. Liu, Recent Advances in Self-Powered Sensors Based on Ionic Hydrogels, Research 8 0571. https://doi.org/10.34133/research.0571.

[50] H. Ma, S. Li, S. Wang, W. Yang, J. Han, Biomimetic All-Wood Sponge for the Co-Generation of Adsorption-Based Atmospheric Water Harvesting and Hydrovoltaic Power Generation, Research 9 1195. https://doi.org/10.34133/research.1195.

[51] F. Yang, P. Peng, Z.-Y. Yan, H. Fan, X. Li, S. Li, H. Liu, T.-L. Ren, Y. Zhou, Z. L. Wang, D. Wei, Vertical iontronic energy storage based on osmotic effects and electrode redox reactions, Nat. Energy 9 (2024) 263–271, https://doi.org/10.1038/s41560-023-01431-4.

[52] H. Qian, D. Wei, Z. Wang, Bionic iontronics based on nano-confined structures, Nano Res. 16 (2023) 11718–11730, https://doi.org/10.1007/s12274-023-5705-z.

[53] L. Xiang, W. Zhong Lin, W. Di, Iontronic logic control driven by dynamic electrical double layer regulation, Iontronics 1 (2025) 2, https://doi.org/10.20517/iontronics.2025.02.

[54] X. Li, Z.L. Wang, D. Wei, Scavenging energy and information through dynamically regulating the electrical double layer, Adv. Funct. Mater. 34 (2024) 2405520, https://doi.org/10.1002/adfm.202405520.

[55] X. Li, R. Li, S. Li, Z.L. Wang, D. Wei, Triboiontronics with temporal control of electrical double layer formation, Nat. Commun. 15 (2024) 6182, https://doi.org/10.1038/s41467-024-50518-3.

[56] X. Li, S. Li, X. Guo, J. Shao, Z.L. Wang, D. Wei, Triboiontronics for efficient energy and information flow, Matter 6 (2023) 3912–3926, https://doi.org/10.1016/j.matt.2023.08.022.

[57] P. Peng, Z.L. Wang, D. Wei, Modulating multi-ion dynamics for high-performance iontronic systems, Iontronics 2 (2026) 5, https://doi.org/10.20517/iontronics.2026.05.

[58] X. Li, G. Amaratunga, Z.L. Wang, D. Wei, Unlocking interfacial charge at dielectric solid–liquid interfaces via triboelectric nanogenerator probe, SmartSys 2 (2026) e70019, https://doi.org/10.1002/sys3.70019.

[59] Y. Long, B. Zhao, M. Liu, W. Hu, X. Pu, Smart hydrogel tactile sensors and systems: a comprehensive review, SmartSys 1 (2025) e70015, https://doi.org/10.1002/sys3.70015.

[60] H. Qian, H. Fan, P. Peng, Y. Du, X. Li, Y. Liu, F. Yang, Y. Zhou, Z.L. Wang, D. Wei, Biomimetic Janus MXene membrane with bidirectional ion permselectivity for enhanced osmotic effects and iontronic logic control, Sci.Adv. 11 eadx1184. https://doi.org/10.1126/sciadv.adx1184.

[61] Y. Ouyang, X. Li, Y. Du, Y. Zhang, Z.L. Wang, D. Wei, Mechano-driven neuromimetic logic gates established by geometrically asymmetric hydrogel iontronics, Small 21 (2025) 2409998, https://doi.org/10.1002/smll.202409998.

[62] X. Li, Y. Wei, X. Gao, Z. Zhang, Z.L. Wang, D. Wei, Harnessing triboiontronic Maxwell's demon by triboelectric-induced polarization for efficient energy-information flow, Joule 9 (2025), https://doi.org/10.1016/j.joule.2025.101888.

[63] J. Liu, Z. Yang, S. Li, H. Qian, T. Gan, N. Wu, Z.L. Wang, D. Wei, Modular contact-electro-chemistry based on dielectrics with work function-tunable metal coatings, Nano Energy 144 (2025) 111389, https://doi.org/10.1016/j.nanoen.2025.111389.

[64] Y. Wang, J. Zhang, W. Zhang, J. Yao, J. Liu, H. He, C. Gu, G. Gao, X. Jin, Electrostatic field in contact-electro-catalysis driven C−F bond cleavage of perfluoroalkyl substances, Angew. Chem. Int. Ed. 63 (2024) e202402440, https://doi.org/10.1002/anie.202402440.

[65] X. Dong, Z. Wang, Y. Hou, F. Yawei, A. Berbille, H. Li, Z. Wang, W. Tang, Regulating contact-electro-catalysis using polymer/metal janus composite catalysts, J. Am. Chem. Soc. (2024), https://doi.org/10.1021/jacs.4c07446.